Appl. Phys. B 68, 305–313 (1999)

Applied Physics B
Lasers
and Optics

Invited paper

Coherent phonon and electron spectroscopy on surfaces using time-resolved second-harmonic generation

H.W.K. Tom, Y.M. Chang, H. Kwak

Department of Physics, University of California, Riverside, CA 92521-7502, USA
(Fax: +1-909/787-4529, E-mail: Harry.Tom@UCR.edu)

Received: 13 October 1998

Abstract. We demonstrate new time-domain surface phonon and surface electronic spectroscopies. We excite coherent surface optical phonons with an ultrashort laser pulse and probe the free-induction decay with time-resolved surface second-harmonic generation (TRSHG). For both clean GaAs(110) and (100) surfaces, the signals are remarkably large and we obtain an energy resolution of 1%, which is comparable to or better than that in HREELS and HAS. The phonon modes must be Raman active to be driven and hyper-Raman active to be detected through TRSHG. We obtain time-domain coherent electron spectroscopy through analysis of the pump–probe cross-correlation SH and a novel superposition of the cross-correlation and probe SH fields proportional to $E_{\mathrm{pump}}(\omega)E^{*}_{\mathrm{probe}}(\omega)\left|E_{\mathrm{probe}}(\omega)\right|^{2}$. This is much easier to detect than transient grating, photon echo, or four-wave mixing schemes that use higher-order nonlinearities. We have applied this technique to measure the energy gap and dephasing time of the dangling bond interband transition on the GaAs(110)-relaxed (1×1) surface. Surface-carrier/surface-phonon interaction plays an important and perhaps dominant role in surface carrier dephasing consistent with the larger electron-phonon coupling on the surface compared to the bulk.

PACS: 68.35.Ja; 78.47.+p; 73.20.-r

Since the advent of the laser, coherent optical spectroscopies have been developed in order to study media which have signals too small to study by traditional absorption or scattering spectroscopies [1]. In general, the laser drives a polarization in the medium which is a coherent superposition of states and the amplitude or relaxation time of that coherence is measured. In frequency-domain techniques, the laser is tuned through resonance with an optical transition. In time-domain techniques a short pump pulse excites an initial superposition of states and a probe pulse detects the free-induction decay of the superposition. Here we present two time-domain coherent spectroscopies suited to measuring phonon and electronic spectroscopy of surfaces and interfaces. The new spectroscopies are based on pump–probe time-resolved second-harmonic generation (TRSHG). Because they are all-optical techniques they have an advantage over particle probes (electron energy loss spectroscopy, helium atom spectroscopy, and photoemission spectroscopy) because they may be used at buried interfaces. On the other hand, they have the limitations of optical techniques, so they can only probe $k\sim 0$ phonons and a superposition over all vertical optical transitions. Even with these limitations, a new technique sensitive enough to use on a variety of surfaces is a welcome and useful addition to surface science. The number of systems for which low-frequency vibrational spectroscopy is available is in fact quite small and electronic lifetime and dephasing dynamics on surfaces is of great current interest. We present experiments on the GaAs-native oxide interface and on clean GaAs(100) and (110) surfaces in UHV. At this point there is every indication these techniques can be used on other semiconductor surfaces.

1 Coherent optical phonon spectroscopy

Currently the most widely used techniques for surface phonon spectroscopy are He atom scattering (HAS) [2] and high-resolution electron-energy-loss spectroscopy (HREELS) [3]. Both are surface sensitive and can probe the entire surface Brillouin zone. HAS is less useful for optical phonons because it cannot probe energies $>\sim 15$ meV. HAS [4] and HREELS [5] studies of the clean (1×1)-relaxed GaAs(110) surface have been reported. In the impact regime HREELS is sensitive at the monolayer level. In the long-range Coulomb regime, HREELS can also be sensitive to buried interfaces – particularly to interface plasmon modes [6–8]. Raman scattering is generally more applicable at buried interfaces because it is an all optical technique. Raman studies of oxidation of GaAs(100) have been reported and the Raman lines for bulk LO phonons, interface strain-induced GaAs TO phonons, and crystalline As have been detected [9]. Raman scattering from clean (UHV) GaAs surfaces has not been reported but both Raman scattering and resonance Raman scattering have been used to study phonons localized

at the interface between Sb monolayers and GaAs(110) [10, 11]. Optical techniques such as Fourier transform infrared spectroscopy [12] and free electron laser based IR spectroscopy [13] have been used on molecules adsorbed to clean surfaces and may also detect low frequency modes at buried interfaces. The phonon bands of the surrounding media may limit the general usefulness of IR spectroscopy for studies of buried interfaces.

Our new coherent surface optical phonon spectroscopy [14] is based on impulse stimulation of the phonons with a pump pulse and then detection of the free induction decay of the phonon modes by time-resolved second-harmonic generation. It is well known that any transient real or virtual excitation of the electronic system can lead to excitation of vibrational modes through electron-phonon coupling. This is perhaps easiest to envision in molecular systems: stimulated Raman excitation (virtual) and Franck-Condon excitation (real) accelerate atoms from their equilibrium positions in the electronic ground state toward the equilibrium positions in the electronically excited state [15]. For bulk solids, the electron-phonon coupling is relatively weak due to the 3-dimensional delocalization of both the electronic and vibrational excitation modes. For surfaces, we expect the electron–phonon interaction to be intermediate between that for a molecule and 3-d solids due to localization in two dimensions. Lateral surface reconstruction and $\sim 5\%$ vertical displacement of the topmost 1–3 atomic layers of most clean surfaces in ultrahigh vacuum provide a clear manifestation of the relative strength of the electron-phonon coupling at surfaces. By exciting with laser pulses shorter in duration than the vibrational period, the temporally coherent electronic excitation will excite coherent atomic motion, i.e., coherent phonon motion. One has only to find a way to detect this motion. In the early 1990's, Kurz and coworkers [16, 17] and Ippen and coworkers [18, 19] demonstrated the excitation of coherent longitudinal optical (LO) phonons in bulk semiconductors, semimetals, and insulators by using femtosecond laser pulses and their detection by time-resolved linear reflectivity. Here because we are interested in the surface phonons, we detect the free-induction decay of the phonon modes by time-resolved second-harmonic generation (TRSHG). Second-harmonic generation has intrinsic surface sensitivity due to it being dipole-allowed at surfaces and dipole-forbidden in centrosymmetric bulk media. Even in non-centrosymmetric media, SHG has proven to be surface sensitive and the contribution from the bulk can often be eliminated by using special excitation geometries [20].

We discuss the mechanisms for driving the coherent surface phonons after the data are presented. Here we concentrate on the detection. Our experiments are the coherent time-domain analog of stimulated hyper-Raman spectroscopy: we detect the interfacial coherent lattice motion using the differential second-order optical susceptibility tensor, $\partial\chi^{(2)}(2\omega)/\partial Q$, where Q is the lattice displacement vector for the $q = 0$ phonon. The SH electric field is driven by the nonlinear polarization $P_i(2\omega)$ at the surface. The SH susceptibility tensor may be expanded to first order in the phonon displacement:

$$P_i(2\omega) = \left[\chi^{(2)}_{ijk}(2\omega) + \sum_{n,q}\left(\partial\chi^{(2)}_{ijk}(2\omega)/\partial\hat{Q}_{n,q}\right)_0 Q_{n,q}\right] \times E_j(\omega)E_k(\omega)\,. \quad (1)$$

The subscripts i, j, k are the indices of the usual vector projections, $Q_{n,q}$ is the amplitude of the n-th phonon mode with wave vector q, and the differential second-order polarizability is taken with respect to the phonon polarization unit vector and is evaluated at the equilibrium point. In this experiment, we use a laser beam with Gaussian waist around 10 μm and thus can only excite surface modes with wave vector $q_\parallel < 1\,\mu\mathrm{m}^{-1}$. For such small values of $q_\parallel$ we can ignore dispersion. In the harmonic approximation, each mode obeys:

$$\ddot{Q}_{n,q} + \dot{Q}_{n,q}/T_n + \omega_n^2 Q_{n,q} = F_{n,q}/\mu_n\,, \quad (2)$$

where T_n, ω_n, $F_{n,q}$, and μ_n are the mode's dephasing time, resonant angular frequency, external force, and effective mass, and we ignore dispersion for small q. In thermal equilibrium the amplitude of $Q_{n,q}$ is given by Bose–Einstein statistics but there is no coherence between the modes of different q, and the contribution to (1) from each mode branch n is washed out.

However, a coherent force applied to the system can drive modes of different q in phase. In our experiment, the duration of F_n is short compared to the oscillation period and dephasing time. After 100 fs delay time, the excited modes of the same branch oscillate in phase at the same frequency – as if a single mode were excited. We thus expect after 100 fs, the SH polarization to have a time-dependence of:

$$P_i(t) \propto \chi^{(2)}_{ijk}(2\omega) + \sum_n \left(\partial\chi^{(2)}_{ijk}(2\omega)/\partial\hat{Q}_{n,q=0}\right)_0 \times A_n\cos(2\omega_n t + \varphi_n)\mathrm{e}^{-t/T_n}\,, \quad (3)$$

where the q-integrated amplitude of the nth mode is A_n and the initial temporal phase of the mode is φ_n. The SH intensity is proportional to $|P|^2$. Experimentally the oscillatory part of the total SH is small. We can thus ignore terms of order A_n^2 and we expect to fit the oscillatory part of the SH intensity to the form: $S(t) = S_n\cos(2\omega_n t + \varphi_n)\mathrm{e}^{-t/T_n}$, where S_n and φ_n will depend on excitation amplitude and geometry and S_n will depend on detection geometry.

The experiments were carried out either in air or under ultrahigh vacuum conditions (base pressure $< 2\times10^{-10}$ Torr). The GaAs(100) was highly n-doped (3×10^{18} Si/cm^3) and the depletion field was calculated to be 740 kV/cm over the topmost 140 Å. The native oxide covered surface was cleaned with solvents, ending with methanol. The clean GaAs(100)-(4×6) surface was prepared in UHV by cycles of 400 eV Ar^+ ion sputtering to remove the native oxide and thermal annealing at 550 °C for 30 min until Auger electron spectroscopy showed negligible oxygen ($< 1\%$ oxygen) and low-energy electron diffraction (LEED) showed a sharp (4×6) pattern (without $c(8\times2)$ features). The (1×1)-relaxed GaAs(110) surface was similarly prepared with Ar^+ ion sputtering and thermal annealing at 550 °C until a sharp (1×1) LEED was observed. We used the SH intensity as the final indicator that the sample was well prepared–the SH intensity is very sensitive to the surface reconstruction quality and was a maximum when the surfaces gave the sharpest surface phonon features.

The optical experiments were performed using 850 nm, 35 fs laser pulses from a Ti:sapphire Kerr–Lens Modelocked laser oscillator with a ~ 80 MHz repetition rate. The weak probe beam was derived from the pump beam with a beam splitter and the pump beam was passed through a delay line.

The pump and probe pulses overlapped spatially in a Gaussian spot with 10 μm waist on the sample surface at ∼ 45° angle of incidence with a ∼ 3° angular separation in the plane perpendicular to the plane of incidence to separate the beams. The second-harmonic generation of the probe beam was detected as a function of time delay between pump and probe. The SH was always detected in *p*-in and *p*-out geometry. The SH was separated from the fundamental with color and interference filters and detected with a cooled photomultiplier tube (PMT). The pump-induced change in the probe SH was obtained by processing the PMT output with a lockin amplifier synchronized to the mechanical chopping rate of the pump beam. For this laser frequency, the SH measures the nonlinear optical response at the interface and also in the topmost 200 Å of the GaAs bulk due to both a bulk dipole-allowed SH susceptibility and DC-field induced SH in the depletion region. The probe depth is determined by optical phase matching and the optical penetration depth.

Since one of the main advantages of these new all optical techniques is their potential use at buried interfaces we present data from the buried GaAs(100)-native oxide surface first [21]. In Fig. 1 we show the TRSHG measurement from the GaAs(100)-native oxide surface held in air. We see a rapid change at near-zero time delay due to carrier injection and rapid carrier-induced screening of the depletion field. A slow decay follows due to carrier recombination and diffusion dynamics. Ultrafast carrier dynamics in the depletion region is well studied and is known to drive coherent LO phonon oscillations in the bulk [16]. We focus presently on the small oscillation on this background signal (see left inset). The oscillatory part, $S(t)$, is separated from the background by discarding the first 150–200 fs of delay time and Fourier filtering frequencies < 3 THz. The oscillation amplitude is ∼ 10% of the pump-induced TRSHG signal and ∼ 1% of the total probe SHG intensity. Because this data is obtained over many scans, it is clear that the oscillation is coherent with the arrival of the pump pulse and due to excitation of coherent phonons. In the right inset of Fig. 1, we show the Fourier power spectrum of $S(t)$ (square of the Fourier transform). The complex Fourier transform of $S(t)$ on an infinite time interval is the sum of complex Lorentzians, however, the complex Fourier transform over a finite time interval has spectral artifacts. We suppress those artifacts by using an apodizing function of the form $[\sin(t-t')]/(t-t')$ with width chosen to minimally impact the phonon features. When we fit the data we iteratively compare the time-domain data with $S(t)$ and the apodized complex Fourier transform of the data and $S(t)$ over the same finite time interval.

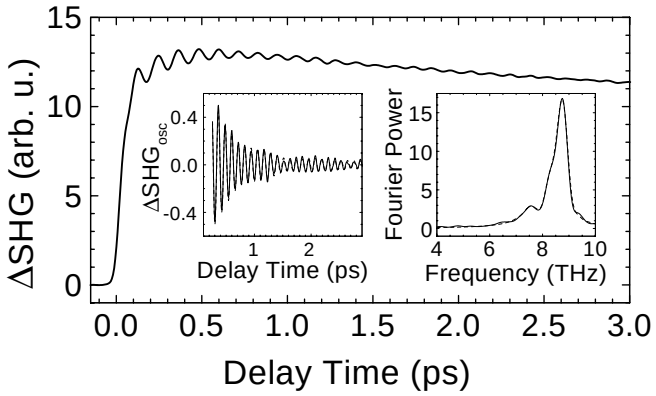

Fig. 1. TRSHG signal for native oxide-covered GaAs(100). The injected carrier density was 7.2×10^{17} /cm^3. Left and right insets show the oscillatory part of the time domain data and the Fourier power spectrum of the oscillatory part. Data (*solid*) and fit (*dashed*)

In Fig. 2, the Fourier power spectra of the TRSHG oscillation data for the native oxide covered GaAs(100) is shown as the injected carrier density is increased (i.e., increasing pump intensity). The photoinjected carrier density at the sample surface is calculated using the literature values of the optical constants integrated over the measured frequency bandwidth of our femtosecond laser pulse. We fit the data for three modes which are clearly visible in the spectra. We find that as the carrier density increases the lowest frequency mode shifts from 7.52 to 7.67 THz, while the middle frequency mode shifts from 8.48 to 8.29 THz, and the highest frequency mode stays at 8.80 ± 0.015 THz. The quality of the fit is not noticeably effected when we fit all curves simultaneously and constrain the frequencies of those two modes to be fixed. The amplitudes of the three modes are shown in the inset. The 8.78 THz mode is the well-known long wavelength bulk LO phonon mode. The amplitude is saturated because it is driven by rapid screening of the depletion field and the injected carrier density is large enough in all cases to screen the field. The ∼ 8.4 THz mode grows linearly with the pump intensity and is therefore not driven by field screening. The maxima of the ∼ 8.4 and 8.8 THz modes seem to both shift and grow as a function of injected carrier density-this is however a result of the coherent superposition of the two features. The two modes are 50° phase shifted from each other so the low-frequency dispersive tail of the bulk LO phonon mode susceptibility is selectively amplified by coherent addition with the susceptibility of the ∼ 8.4 THz mode. The mode that shifts from 7.52 to 7.67 THz is the well-known bulk LO phonon–electron plasmon coupled mode. Both bulk modes have been observed and studied by Kurz and coworkers [17, 22].

The mode at ∼ 8.4 THz is a local interfacial mode confined to a few monolayers of the interface. It cannot be a pure bulk mode because no $q \sim 0$ phonon modes exist between the TO and LO frequencies of 8.0 and 8.8 THz. This mode cannot

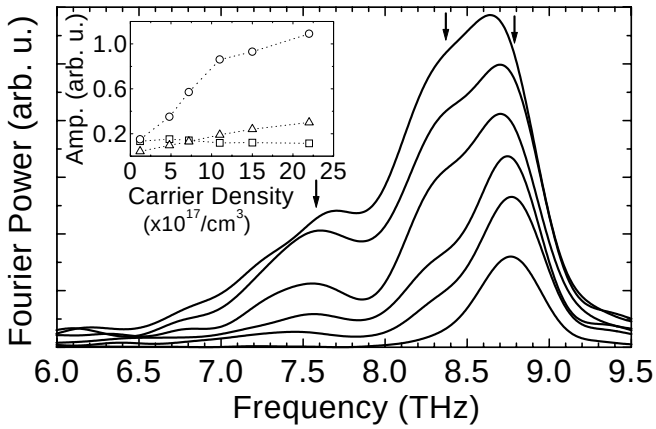

Fig. 2. Fourier power spectra of the TRSHG of native oxide-covered GaAs(100). From *bottom to top curve* peak injected carrier densities were: 1.2, 4.8, 7.2, 11, and 22($\times 10^{17}$ /cm^3). *Arrows* and *symbols* indicate center frequencies for the bulk LO phonon (□ 8.78 THz), interface phonon (○ 8.36 THz), and bulk LO-electron plasma coupling mode (△ 7.62 THz). Inset: mode amplitude vs. carrier density

be the Fuchs-Kliewer (F-K) or interface plasmon mode at the oxide/semiconductor interface that dominates HREELS [23]. The Fuchs-Kliewer (F-K) mode is a delocalized mode with a displacement vector that varies sinusoidally along the surface and exponentially into the bulk as $\exp(iq_{\parallel}x - q_{\parallel}z)$ [24]. The laser spot size only allows excitation of modes with $q_{\parallel} < 1\,\mu\text{m}^{-1}$ and therefore any excited modes would extend $> 1\,\mu$m into the bulk. First, if we detected the F-K mode we would expect the mode frequency and dephasing time to depend on the injected carrier density as observed for the bulk LO-electron plasmon coupled mode. In fact, after carefully subtraction of the bulk LO phonon mode, the mode is observed to shift from 8.48 to 8.29 THz over the full range of injected carriers. This is much less than would be expected for any bulk LO-phonon-hole plasmon coupled mode or bulk LO-phonon-electron plasmon coupled mode. Second, the SH suppresses detection of the F-K mode by > 50 compared to HREELS because the excitation is spread over $> 1\,\mu$m while the SH is only able to detect perturbations in the topmost 200 Å. HREELS is able to both excite modes of larger q and couple strongly to modes localized closer to the surface. We must conclude that the ~ 8.4 THz mode is localized to a few monolayers at the native oxide-GaAs interface.

In Fig. 3 we show the Fourier power spectra of the oscillatory TRSHG signals from the clean GaAs(100)-(4×6) for different oxygen exposures. Oxygen was backfilled into the chamber in the presence of a lit nude ion gauge filament. Adsorption of O atoms produced by cracking molecular O_2 at the hot filament is known to proceed efficiently. After 100 L of exposure (curve B) there are significant changes in the surface phonon spectrum. The native oxide data (curve E) was measured in the UHV chamber with nominally identical laser conditions as for curves A–D but before the oxide

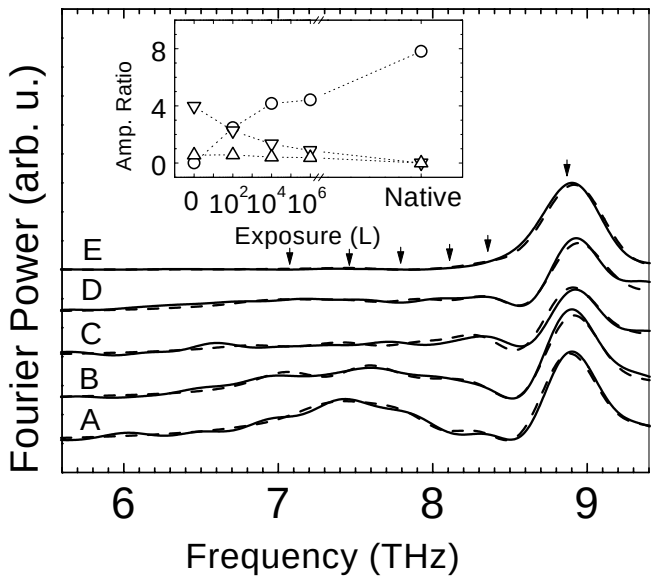

Fig. 3. TRSHG Fourier power spectrum for oxygen on GaAs(100)-(4×6) with O_2 exposures (Langmuir): (A) clean surface, (B) 10^2 L, (C) 10^4 L, and (D) 10^6 L, (E) native oxide covered surface in UHV chamber. The injected carrier density was 1.2×10^{17} /cm^3. Fourier transform of data (*solid*) and curve fitting result (*dashed*). *Arrows* indicate fit center frequencies at 7.1, 7.54, 7.83, 8.15, 8.36 and 8.8 THz. Inset: surface/bulk LO phonon amplitude ratio for selected modes – (△ 7.54 THz, ▽ 7.83 THz, and ○ 8.36 THz)

was removed and the surface was cleaned. The laser intensity is reduced to eliminate the LO phonon–electron plasmon coupled mode (i.e., the 7.52–7.67 THz mode in Fig. 2). In comparing curves A and E, we see new phonon modes that must be localized to the 1–3 monolayers of the surface reconstruction. The progression from curve A to curve D clearly establishes the chemical sensitivity of this technique and is consistent with the assignment of the phonon modes being localized to the reconstructed layers.

Here the modes are not as easily recognized by eye as in Fig. 2. Arrows indicate the center frequency of the optical phonon modes obtained by fitting the data. In addition to iterative fitting of the time domain data and derived complex Fourier transforms, we also constrained the fitting process by requiring the mode frequencies to be the same for traces A–E and we added modes until all traces had reasonable fits. S_n, T_n, and φ_n were allowed to vary for the five traces.

In the inset we show the amplitudes of several of the phonon modes as a function of oxygen coverage where we take the native oxide to be infinite exposure. The phonon mode amplitudes are normalized to the bulk LO phonon mode at 8.78 THz. Four surface/interface modes detected in curve A decrease while a fifth mode at 8.36 THz grows continuously with oxidation. The apparent sharp zero in Curve A at ~ 8.5 THz is due to the nearly destructive interference of the LO phonon peak at 8.78 THz and a surface phonon at 8.15 THz. As the surface is oxidized, the amplitude of the 8.15 THz mode decreases and the 8.36 THz mode increases. The 8.36 THz mode adds constructively to the LO phonon mode so the LO phonon mode looks broader on the low frequency side. When we subtract the LO phonon peak at 8.80 THz, we find that the 8.36 THz mode present at 100 L shifts toward 8.5 THz between D and E. It is significant that the mode at 8.36 THz has appreciable amplitude even at 100 L exposure at which coverage one expects that oxidation has only occurred on a fraction of the dangling bonds. The mode must be highly localized within the first 1–3 layers of the interface and could involve atoms bonded directly to oxygen atoms or atoms under stress due to the oxide layer. In principle the mode frequencies could shift since we cannot distinguish between the decrease of the 8.15 THz mode and increase of a new 8.36 THz mode and the gradual shift of a mode from 8.15 to 8.36 THz. However, because the modes have nearly opposite phase suggests they have different displacements and are probably distinct modes. On the native oxide interface, the linewidth of the ~ 8.4 THz mode is $< 2\times$ broader than that of the bulk LO phonon indicating that the interfacial phonon is not strongly broadened by inhomogeneities. Since the native oxide of GaAs(100) is known to be disordered and non-epitaxial, we can argue that it is unlikely that the mode is due to stretching modes of the top most Ga−O atomic layers. The most likely assignment is motion of the second and third atomic layers below the semiconductor-oxide interface at a frequency shifted from the bulk by oxidation-induced stress or strain. It is also possible that the mode is always present but is only brought into resonance with the laser when oxidation induces a different interfacial electronic structure. Recently, SH has been shown to be enhanced at the Si/SiO_2 interface due to resonant enhancement with the E_2 state induced by the interfacial strain [25, 26]. There is no reason to preclude such effects for GaAs.

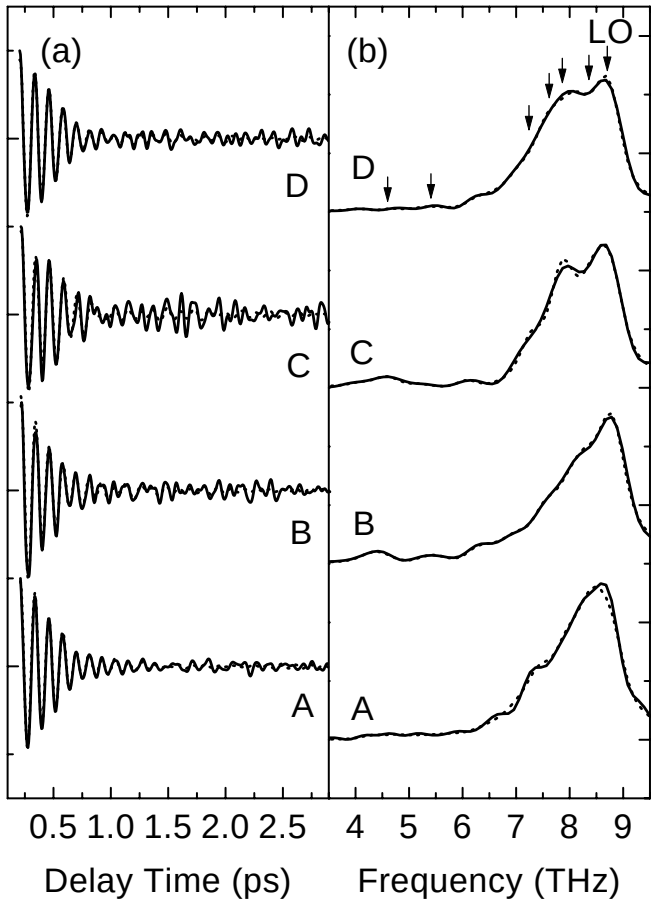

Fig. 4a,b. Differential p_{in}-p_{out} TRSHG for GaAs(110)-(1×1) surface. **a** Oscillatory part and **b** Fourier power spectra of differential p_{in}-p_{out} TRSHG for 4 geometries. A: [001] ∥ plane, *s*-pol. pump. B: [001] ∥ plane, *p*-pol. pump. C: $[1\bar{1}0]$ ∥ plane, *s*-pol. pump. D: $[1\bar{1}0]$ ∥ plane, *p*-pol. pump. Data in *solid lines* and results of curve fitting in *dotted lines*. *Arrows* show phonon frequencies obtained from fit

In Fig. 4 we show TRSHG data for the GaAs(110)-relaxed (1×1) surface [14]. We studied this system because we can compare our results to published theoretical calculations and HREELS studies. Figure 4a shows the oscillatory part of the TRSHG data for 4 excitation geometries where the sample is oriented with either the crystalline $x=[001]$ or $y=[1\bar{1}0]$ axes parallel to the plane of incidence, and for the pump pulse either *s*- or *p*-polarized. Figure 4b shows the power spectra. The dotted lines are the fits and the ν_n values are indicated with arrows in Fig. 4b. The apparent maxima in the power spectra are shifted from ν_n by interference with neighboring modes. We fit all 4 curves simultaneously constraining ν_n and T_n to be fixed. The fit values are listed in Table 1. The fits to the data are excellent and the constraint of fitting 4 curves simultaneously gives us an error bar $<\pm0.1$ THz despite the large number of free parameters. Our frequency resolution is better than in HREELS (±1 meV $=0.25$ THz) which is an important advantage particularly for complicated surfaces with deep reconstructions or large unit cells.

Table 1. Fit results and symmetry of surface phonons observed on GaAs(110)-relaxed (1×1) and previous HREELS and theoretical values

n	ν_n /THz	T_n /fs	Sym.	Exp't [5]	Theo [27]	Theo [28]
	8.76 ± 0.01	740 ± 80		8.76	bulk LO	
1	8.35 ± 0.07	800 ± 30	A'		8.36	
2	7.85 ± 0.01	470 ± 10	A'		7.86	
3	7.58 ± 0.01	720 ± 50	A'		7.56	
4	7.29 ± 0.03	550 ± 30	A'		7.37	
5	5.41 ± 0.04	600 ± 150	A'/A''	5.5 ± 0.25	5.80	5.32 5.56
6	4.57 ± 0.05	790 ± 140	A'	3.9 ± 0.4	3.98	3.94

The bulk LO phonon mode is present at 8.76 THz. All the other modes (1–6) we observe are due to surface phonon modes localized to the topmost 3 reconstructed layers. The symmetry of the hyper-Raman tensor allows us to deduce the symmetry of the modes by measuring the SH in different excitation geometries. The (110) surface has *m* symmetry and modes are either A' (symmetric) or A'' (antisymmetric) upon mirror reflection in the *xz* plane. Only A' modes can be detected by SH when the $x=[100]$ axis is in the plane of incidence. Appearance of a mode allows us to identify it as A'. Both A' and A'' modes can be detected when the $y=[1\bar{1}0]$ axis is in the plane of incidence. The appearance of a mode only in this geometry is necessary but not sufficient to identify it as A''. The mode identifications are noted in Table 1.

In Table 1 we also list values of mode frequencies from HREELS data [5], an ab initio calculation [27], and a tight-binding total-energy minimization model calculation [28]. We observe one mode at 8.35 THz and three modes between 7–8 THz which are predicted in the ab initio calculation to be dominated by the opposing motion of the topmost Ga and second layer As perpendicular to the chains and opposing Ga-As motion in layers 2 and 3 parallel to the plane, respectively. The agreement with theory is extraordinary but may be simply due to there being 4 modes within a narrow frequency range. These 4 modes are not observed in HREELS–perhaps because they are largely polarized in the plane or because the F-K mode obscures these modes in HREELS. As discussed above, the F-K mode is suppressed in TRSHG compared to HREELS.

The mode at 5.41 THz matches the value measured in HREELS and is in relatively good agreement with the value 5.80 THz predicted in the ab initio calculation for the motion of the topmost As atom perpendicular to the chain. Our measured value agrees better with the tight-binding model calculation in which there are two shear modes of the topmost Ga and As atoms parallel ($1A''$ at 5.32 THz) and perpendicular ($3A'$ at 5.56 THz) to the zigzag chain direction. Interestingly, the only mode that we detected that could have A'' symmetry is the 5.41 THz mode.

We also measure a mode at 4.57 THz that is just outside the range of 3.9 ± 0.4 THz of the HREELS measurement. The ab initio calculation predicts a mode at 4 THz dominated by motion of the topmost Ga atom perpendicular to the chain. The tight-binding calculation predicts a bond-length preserving rotation of the topmost Ga and As atoms in the direction perpendicular to the chain, also at 4 THz. We may be detecting the same mode as in the HREELS measurement or may be detecting an additional mode that is dominated by in plane motion and therefore suppressed in HREELS.

The force F_n that drives the coherent optical phonons can be due to 4 general mechanisms. The first two involve rapid

increases in carrier density leaving the atoms suddenly in vibrationally excited positions with respect to new equilibrium positions. Ippen and coworkers have called this mechanism Displacive Excitation of Coherent Phonons (DECP) [18, 19] when the carrier density changes the magnitude of the atomic bonding strength. This change is equivalent to changing the equilibrium lattice constant so only fully symmetric A' modes can be excited. A second mechanism applies for semiconductors with a built-in surface electric field that induces static LO phonon displacement. When the injected carriers rapidly screen the field, the lattice is suddenly free to oscillate about the field free (or lower field) lattice equilibrium positions. Kurz and coworkers have shown this is the dominant mechanism for exciting the bulk LO phonons in the depletion region of GaAs [16, 17]. A third driving mechanism is Stimulated Raman Excitation (SRE). The force is $F_n = \frac{1}{2}\varepsilon_0 |\partial\alpha^{(1)}/\partial Q_n|_0 : EE^*$, where the differential linear polarizability per unit cell is evaluated at the equilibrium point and is related to the Raman scattering cross-section, and E is the laser electric field. This mechanism dominates coherent vibrational excitation of molecules and molecular crystals [15]. The fourth driving mechanism is vibrational excitation through electronic excitation and rapid de-excitation, i.e., the Franck–Condon effect for molecules or the generalized Menzel-Gomer-Redhead (MGR) type mechanism for surfaces [29]. The atoms accelerate while briefly in the electronically excited state and return to the ground electronic state vibrationally excited. Both SRE and MGR have Raman selection rules. In all four mechanisms, excitation of a large coherent phonon oscillation is possible only because the laser pulse is short.

Examination of the A-B and C-D pairs of data in Fig. 4 shows that when the pump laser is changed from *s*- to *p*-polarization the SH signal is different for all surface modes. Only SRE and MGR mechanisms can depend on the polarization of the laser beam – DECP and "field screening" depend only on the number of electrons excited. Thus all surface modes we detected were driven by SRE or MGR mechanisms.

The detected signal amplitude is proportional to the driving term, which for both SRE and MGR scales as the Raman susceptibility and to the sensitivity of SH detection via the hyper-Raman susceptibility. Because both tensors are unknown, it is premature to infer specific information about the relative amplitudes of various surface modes. However, it is very clear that the SH oscillation signals for the coherent surface phonons are extraordinarily large–the same order of magnitude as that for the bulk LO phonons. We calculated the bulk LO phonon amplitude to be 0.01 Å over ~ 50 Å depth [17]. The surface phonons must be localized to ~ 5 Å–10 times fewer atomic layers. Moreover, the Raman cross-section per layer for the bulk is 40 times too small to produce the same amplitude generated by field screening. The ratios of the two susceptibilities and the peak displacements must give a factor of 400 enhancement for the surface. We expect some enhancement compared to the bulk because the electron–phonon interaction is stronger due to 2d confinement. We have also found that the SH is enhanced at the laser fundamental by resonance with the highest lying occupied dangling bond to lowest lying unoccupied dangling bond interband transition [30]. A 20× enhancement in both tensors is therefore reasonable. So despite the large signal, the surface atomic displacement is likely only ~ 0.005 Å.

The observation that the driving mechanism is generally applicable (i.e., Raman susceptibility or Franck–Condon effect) suggests that this technique may be used on other surfaces. Although the clean GaAs surface results are resonantly enhanced, the results on the native oxide covered surface are not. It is thus likely that this technique can be used on many semiconductor surfaces and we are currently exploring if this technique is sensitive enough to use on metal and insulator interfaces.

2 Coherent surface electronic spectroscopy

The same femtosecond time-resolved SHG setup used for coherent phonon spectroscopy can be used for a novel time-domain coherent surface electronic spectroscopy [31]. The basic geometry of pump–probe excitation on the surface is shown in Fig. 5. Instead of measuring only the SH field produced by the probe beam, we detect both the pump–probe cross-correlation SH intensity and the SH intensity produced by the interference between the pump–probe cross-correlation SH field and the usual probe SH field. In the plane-wave approximation the cross-correlation and probe-only SH fields have different wave vectors and do not interfere. However for small Gaussian beams intersecting at small angles, diffraction provides a range of wave vectors over which they may interfere in the far field. This is suggested graphically in Fig. 5 by the shaded region for the combined source polarization. In practice the weak cross-correlation SH field radiation is heterodyned with the larger probe-only SH field and is thus best detected closer to the probe-only SH beam than halfway between the cross-correlation and probe-only beams.

Recently coherent spectroscopy of surface electronic states has been accomplished by interferometric 2-photon photoemission [32]. This detects real population created by two photon absorption and is thus proportional to the square of pump and probe fields. That technique has the distinct advantage over this all-optical technique of selection within *k*-space. The optical technique described here has the advantage that it can in principle be used at buried interfaces.

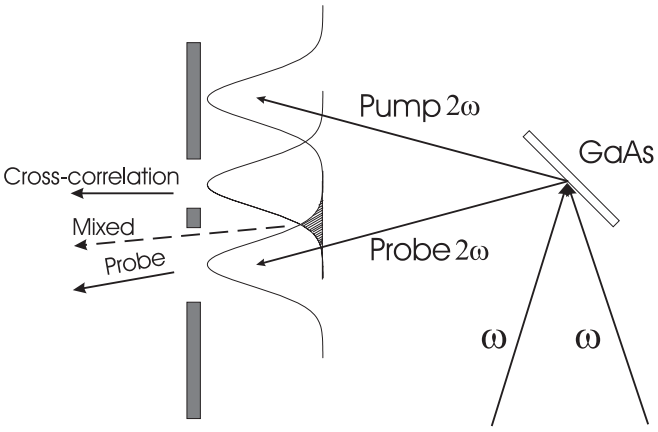

Fig. 5. Pump–probe beam geometry for surface SHG with small Gaussian beams

As we will discuss below, it is based on the second-order nonlinearity and is thus quite similar to two-photon absorption. It therefore has signal to noise advantages over surface photon echoes or other higher-order nonlinear wave-mixing techniques.

We consider the case of a 3 level system when the laser fundamental frequency is nearly resonant with the optical transition between lower levels 1 and 2. The time evolution of the density matrix can be solved in the presence of two time-delayed pump and probe electric fields. Using subscripts pump and probe to designate the matrix elements driven by the pump and probe fields, the off-diagonal element $\rho_{31}(t, 2\omega) \propto (\rho_{21,\mathrm{pump}} + \rho_{21,\mathrm{probe}})(E_{\mathrm{pump}} + E_{\mathrm{probe}})$. The cross-correlation SH field $E_{x-\mathrm{corr}}(2\omega, t) \propto \rho_{21,\mathrm{pump}} E_{\mathrm{probe}} + \rho_{21,\mathrm{probe}} E_{\mathrm{pump}}$ and the probe-SH field $E_{\mathrm{probe}}(2\omega, t) \propto \rho_{21,\mathrm{probe}} \times E_{\mathrm{probe}}$. Since $\rho_{21}(t)$ is a driven wave, the finite response of the system due to both dephasing and the frequency detuning between the two level resonance and the laser fundamental frequency will broaden and shape the cross-correlation compared to the true autocorrelation of the pump and probe laser fields. If the laser fields are known exactly, for example from a Frequency-Resolved Optical Gating (FROG) measurement [33], one can deconvolve the measured cross-correlation data and deduce dephasing times that are as short or even shorter than the laser pulse duration. On the other hand, most investigators use the cross-correlation measurement as the autocorrelation to diagnose their pulse duration. In UHV chambers with optical windows, it becomes especially difficult to irradiate samples with transform limited pulses. It thus becomes necessary to obtain a second measurement (like FROG) which will constrain the fitting procedure so both $E(t)$ and $\rho_{21}(t)$ can be deduced. We choose as our second measurement the radiation produced by the probe-SH field with a small amount of pump–probe cross-correlation signal added by diffraction. The SH intensity of this signal is $I(2\omega, t) \propto |E_{\mathrm{probe}}(2\omega, t) + \beta E_{x-\mathrm{corr}}(2\omega, t)|^2$. This signal intensity can be split into the usual probe-SH intensity $I_{\mathrm{probe}}(2\omega, t)$ plus the intensity due to the cross-term $I_{\mathrm{mixed}}(2\omega, t) \propto E_{\mathrm{pump}} E^*_{\mathrm{probe}} |E_{\mathrm{probe}}|^2$. $I_{\mathrm{mixed}}(2\omega, t)$ oscillates as $\cos(\sim \omega t_{\mathrm{d}})$ where t_{d} is the pump–probe delay time. It is also asymmetric with respect to zero time-delay if the laser pulse is asymmetric or the material response is finite. The term proportional to β^2 can always be made small enough to neglect.

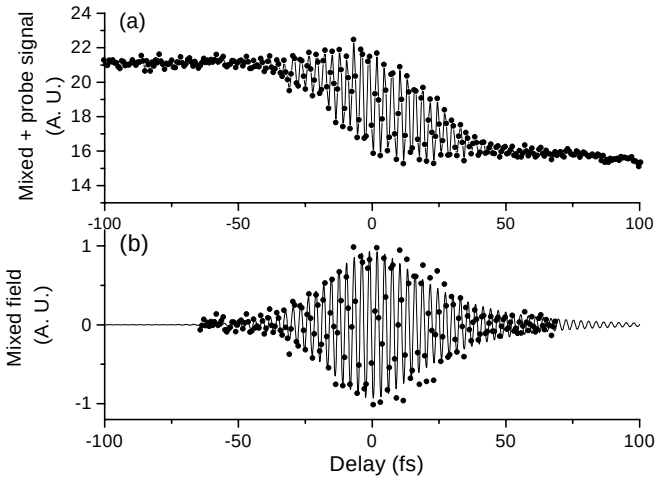

Fig. 7a,b. Pump-induced probe SH field with pump–probe cross-correlation SH field mixed in by diffraction. **a** Data in *circles*, *solid line* is a guide to the eye. **b** Probe-SH and cross-correlation SH interference term after background subtraction and normalization. Data in *circles* and *solid line* is a fit

In Fig. 6 we show the pump–probe cross-correlation signal measured on the clean GaAs(110)-relaxed (1×1) surface in UHV at 4 temperatures. We see immediately that the width of the cross-correlation is different at the 4 temperatures. The laser center wavelength was 857 nm. Assuming the laser parameters are the same, the result can only be explained by the temperature dependence of the surface electronic system.

The cross-correlation alone, however, is not enough to know whether this system can even be described as 3 level system in which there is a 1 photon resonance with the two lower levels. In Fig. 7a we show the probe and mixed SH intensity as a function of delay time for the sample at 183 K. Oscillations are clearly present. The rapid change in the average SH level are due to carrier injection and field screening dynamics as discussed earlier in this paper. In Fig. 7b, we show the renormalized mixed SH intensity where we have first subtracted the oscillations from the rapidly changing background and then renormalized for the changing background. The oscillation amplitudes are clearly asymmetric with respect to zero time delay. Both cross-correlation and probe/mixed SH were measured simultaneously to establish the zero of time delay.

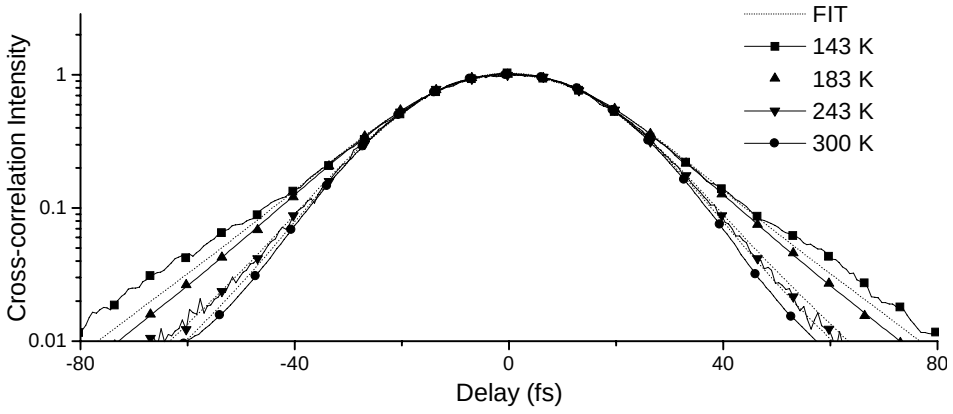

Fig. 6. Pump–probe cross-correlation SH Intensity vs. delay time generated on the GaAs(110)-relaxed (1×1) surface in UHV at various temperatures. Data in *solid lines* with marks and fits in *dashed lines*

The resulting curve is then fit using the 3-level system model of the material characterized by a single gap energy E_g and dephasing time T_2. The solid curve in Fig. 7b and the dashed curves in Fig. 6 are results of the fit. The laser pulse electric field is taken to be a chirped sech pulse, that is, the pulse envelope is calculated by inverse Fourier transform of a frequency spectrum $g(\omega-\omega_0) = g_0(\omega-\omega_0)\exp(i\varphi'''(\omega-\omega_0)^3/6)$ with $g_0(\omega-\omega_0)$ being the transform limited spectrum of the pulse envelope $E_0(t) = \sec h(t/\tau)$. We found that the values of φ''' and τ were relatively close when we fitted each temperature pair of data separately so we further constrained the laser pulse parameters by simultaneously fitting all 4 temperature sets of data (8 curves in all). We found excellent agreement using $\tau = 9.48$ fs, $\varphi''' = 3512.46\,\text{fs}^3$, $E_g = 1.4292$, 1.4272, 1.4441, and 1.4501 eV, and $T_2 = 27.11$, 24.74, 18.14, 15.69 fs for the temperatures 143 K, 183 K, 243 K, and 300 K respectively. We included only 3rd-order dispersion in this analysis. We found that including higher-order dispersion did not significantly improve the fits or change E_g and T_2.

The success of the fit especially in the interference pattern is consistent with 1-photon resonance with a 2 level system and no 2-photon resonance. The 1-photon resonance is due to the dangling bond highest occupied to lowest unoccupied interband transition. Ab initio calculations [30] show these bands to be relatively flat with ~ 1.5 eV gap energy and that both bands overlap bulk bands near the surface Γ-point. The precision of E_g is high because the interference period is sensitive to the detuning between the driven and laser frequencies. However, the absolute accuracy is limited by the laser center frequency which in this measurement is only 3 digits. The measurement can in principle sample all parts of the band, however, the measurement is most sensitive to states with longest dephasing time (away from the Γ-point) and also those with the largest density of states near inflection points in the band. It is thus likely that we measure the coherence of states near the minimum direct gap between the dangling bond bands. The apparent increase in dangling bond gap energy at increased temperature is exactly opposite to what occurs for the bulk band gap of GaAs.

In Fig. 8, we plot the dephasing rate $(1/T_2)$ vs temperature for the four temperatures. We were not able to detect a change in dephasing time when we increased the pump intensity by factors of 2 and 4. We thus conclude that surface carrier-injected carrier coupling does not dominate the dephasing for this range of excitations. The only other possibilities are surface carrier-bulk carrier coupling and surface carrier-surface phonon coupling. We can eliminate surface carrier-bulk phonon coupling due to the poor overlap between the two-dimensional surface carrier wave function and the 3-d phonon. The solid line in the figure is a fit to: $T_2^{-1} = W(2n+1)$ where W is the spontaneous electron and hole k-scattering rate due to phonon emission and the occupation number for phonons of frequency ν is $n = [\exp(h\nu/k_BT)-1]^{-1}$. The rate gives equal weight to phonon absorption and emission processes. An excellent fit is obtained with $W = 27.8^{+2.4}_{-3.2}$ THz and $\nu = 5.7 \pm 1.0$ THz where the error bars take into account the relatively large $\pm 5\%$ error bar in the T_2 measurement. This frequency range is consistent with measured surface phonon frequencies. This suggests that surface carrier-surface phonon interaction dominates k-scattering in the dangling bond bands, however, this fit function only applies if the carriers are not at the global band extrema. At the global band extrema, the carriers can only scatter by absorbing a phonon and then the carrier-phonon scattering cross-section would scale as n. The data do not fit $T_2^{-1} \propto n$. In the ab initio surface electronic band structure calculation [30], there is a minimum energy gap at the surface X point at the global minimum for the unoccupied dangling bond but at an intermediate energy for the occupied dangling bond and another energy gap at the surface Γ-point where the states are surface resonances with strong bulk character. The former will have dephasing rate $T_2^{-1} = W_e n + W_h(2n+1)$ where we have allowed for different cross-sections for electron and hole scattering. In both cases, the dephasing rate would fit $T_2^{-1} = B + Cn$. Unfortunately, because we have data for only a small temperature range, the data fits this form equally well for all ν from 2 to 11 THz with B ranging from 25–30 THz. In either case, surface carrier-phonon scattering is an important carrier dephasing mechanism responsible for half the dephasing at room temperature if the coherence is at the Γ-point and even more for other scenarios. We note that this is also just opposite to bulk GaAs where carrier-carrier scattering dominates carrier-phonon interaction by almost an order of magnitude. The carrier-LO phonon coupling time in GaAs is ~ 130 fs. The reduction to ~ 20 fs is consistent with the relative enhancement of electron-phonon interaction expected in 2-dimensions due to electron [34] and phonon confinement [35]. This observation is clearly consistent with the strong carrier-phonon interaction that is needed to generate the large coherent phonon oscillations observed in our TR-SHG experiments.

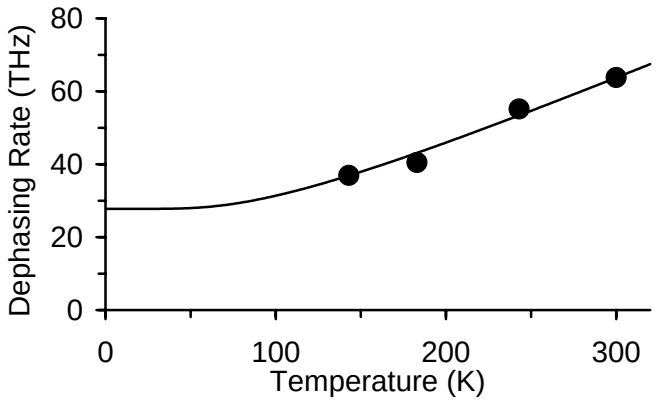

Fig. 8. Dephasing rate vs. temperature. Data in *solid circles*, Fit in *solid line*

3 Conclusion

We have demonstrated the use of two time-domain coherent spectroscopies using time-resolved SHG to obtain phonon and electronic spectra. Since TRSHG has already been shown to be useful in investigations of photo-induced desorption [36] and reaction, these new capabilities make TRSHG a much richer tool for examining photochemically induced phenomena.

Acknowledgements. The authors thank NSF, LBL, and LLNL for partial funding of this research.

References

1. See for example, Y.R. Shen: *Principles of Nonlinear Optics* (Wiley, New York 1984)
2. P. Toennies: J. Vac. Sci. Technol. A **5**, 440 (1987)
3. H. Ibach, D.L. Mills: *Electron energy loss spectroscopy and surface vibrations* (Academic Press, New York 1982)
4. U. Harten, J.P. Toennies: Europhys. Lett. **4**, 833 (1987); R.B. Doak, D.B. Nguyen, J. Electron. Spectrosc. Relat. Phenom. **44**, 205 (1987)
5. H. Nienhaus, W. Mönch: Phys. Rev. B **50**, 11750 (1994)
6. P. Senet, P. Lambin, A.A. Lucas: Phys. Rev. Lett. **74**, 570 (1995)
7. V. Polyakov, A. Elbe, J.A. Schaefer: Appl. Phys. A **60**, 567 (1995)
8. T. Tsuruoka, Y. Uehara, S. Ushioda, T. Kojima, et al.: Surf. Sci. **368**, 185 (1996)
9. N. Levinsohn, R. Beserman, C. Cytermann, et al.: Appl. Phys. Lett. **56**, 1131 (1990): A. Rim, R. Beserman: J. Appl. Phys. **74**, 897 (1993), and references therein
10. M. Hunermann, J. Geurts, W. Richter: Phys. Rev. Lett. **66**, 640 (1991)
11. N. Esser, M. Kopp, P. Haier, A. Kelnberger, W. Richter: J. Vac. Sci. Technol. B **11**, 1481 (1993)
12. R. Ryberg: Phys. Rev. B **32**, 2671 (1985)
13. C.J. Hirschmugl, G.P. Williams, F.M. Hoffmann, Y.J. Chabal: Phys. Rev. Lett. **65**, 480 (1990)
14. Y.M. Chang, L. Xu, H.W.K. Tom: Phys. Rev. Lett. **78**, 4649 (1997)
15. Y.X. Yan, E.B. Gamble, K.A. Nelson: J. Chem. Phys. **83**, 5391 (1985)
16. G.C. Cho, W. Kutt, H. Kurz: Phys. Rev. Lett. **65**, 764 (1990)
17. W.A. Kutt, W. Albrecht, H. Kurz: IEEE J. Quantum Electron. **QE-28**, 2434, (1992), and references therein
18. M.J. Zeiger, S. Vidal, T.K. Cheng, E.P. Ippen, G. Dresselhaus, M.S. Dresselhaus: Phys. Rev. B **45**, 768 (1992)
19. T.K. Cheng, S. Vidal, M.J. Zeiger, G. Dresselhaus, M.S. Dresselhaus, E.P. Ippen: Appl. Phys. Lett. **58**, 980 (1991)
20. T. Stehlin, M. Feller, P. Guyot-Sionnest, Y.R. Shen: Opt. Lett. **13**, 389 (1988)
21. Y.M. Chang, L. Xu, H.W.K. Tom: submitted to Phys. Rev. Lett. B
22. G.C. Cho, T. Dekorsy, H.J. Bakker, R. Hovel, et al.: Phys. Rev. Lett. **77**, 4062 (1996)
23. R. Matz, H. Lüth: Suppl. Le Vide, Les Couches Minces **201**, 762 (1980); L.H. Dubois, G.P. Schwartz: Phys. Rev. B **26**, 794 (1982)
24. R. Fuchs, K.L. Kliewer: Phys. Rev. **140**, 2076 (1965)
25. W. Daum, H.-J. Krause, U. Reichel, H. Ibach: Phys. Rev. Lett. **71**, 1234 (1993)
26. C. Meyer, G. Lupke, U. Emmerichs, F. Wolter, et al.: Phys. Rev. Lett. **74**, 3001 (1995)
27. J. Fritsch, P. Pavone, U. Schröder: Phys. Rev. Lett. **71**, 4194 (1993)
28. T.J. Godin, J.P. LaFemina, C.B. Duke: J. Vac. Sci. Technol. B **9**, 2282 (1991)
29. D. Menzel, R. Gomer: J. Chem. Phys. **41**, 3311 (1964); P.A. Redhead: Can. J. Phys. **42**, 886 (1964)
30. R. Honke, J. Fritsch, P. Pavone, U. Schröder: Phys. Rev. B **53**, 9923 (1996)
31. H. Kwak, K.C. Chou, H.W.K. Tom: submitted to Phys. Rev. Lett.
32. S. Ogawa, H. Nagano, H. Petek, et al.: Phys. Rev. Lett. **78**, 1339 (1997)
33. R. Trebino, K.J. Kane: J. Opt. Soc. Am. A **10**, 1101 (1993): T. Tsang: Phys. Rev. A **52**, 4116 (1995)
34. S. Das Sarma, J.K. Jain, R. Jalabert: Phys. Rev. B **41**, 3561 (1990)
35. B.K. Ridley et al.: In J. Shah: *Hot Carriers in semiconductor nanostructures: Physics and Applications* (Academic Press, New York, 1992)
36. J.A. Prybyla, H.W.K. Tom, G.D. Aumiller: Phys. Rev. Lett. **68**, 503 (1992)